Journal of Materials Chemistry B

Simple, Common but Functional: Biocompatible and Luminescent Rare-Earth Doped Magnesium and Calcium Hydroxides from Miniemulsion

Journal:	*Journal of Materials Chemistry B*
Manuscript ID:	TB-ART-07-2014-001206
Article Type:	Paper
Date Submitted by the Author:	21-Jul-2014

Complete List of Authors:	Butturini, Erika; IENI-CNR Dipartimento di Science Chimiche, Dolcet, Paolo; Università degli Studi di Padova, Department of Chemistry Casarin, Maurizio; Università degli Studi di Padova, Department of Chemistry Speghini, Adolfo; University of Verona, Department of Biotechnology Pedroni, Marco; Università di Verona, Department of Biotechnology Benetti, Filippo; Università degli Studi di Trento, Motta, Antonella; Università degli Studi di Trento, Badocco, Denis; Università degli Studi di Padova, Department of Chemistry Pastore, Paolo; Università degli Studi di Padova, Department of Chemistry Diodati, Stefano; IENI-CNR Dipartimento di Science Chimiche, Pandolfo, Luciano; Universita di Padova, Dept. of Chemical Sciences Gross, Silvia; IENI-CNR Dipartimento di Science Chiriche,

Cite this: DOI: 10.1039/c0xx00000x

www.rsc.org/xxxxxx

ARTICLE TYPE

Simple, Common but Functional: Biocompatible and Luminescent Rare-Earth Doped Magnesium and Calcium Hydroxides from Miniemulsion

Erika Butturini,[a,b] Paolo Dolcet,[a,b] Maurizio Casarin,[a] Adolfo Speghini,[c] Marco Pedroni,[c] Filippo Benetti,[d] Antonella Motta,[d] Denis Badocco,[a] Paolo Pastore,[a] Stefano Diodati,[a,b] Luciano Pandolfo[a] and Silvia Gross*[a,b]

Received (in XXX, XXX) Xth XXXXXXXXX 20XX, Accepted Xth XXXXXXXXX 20XX
DOI: 10.1039/b000000x

Nanostructured (d ~ 20-35 nm) and highly luminescent $Ca(OH)_2$:Ln and $Mg(OH)_2$:Ln (Ln = Eu^{III}, Sm^{III}, Tb^{III}, Mg(Ca)/Ln = 20:1) nanostructures were obtained in inverse (water in oil - w/o) miniemulsion (ME), by exploiting the nanosized compartments of the droplets to spatially confine the hydroxides precipitation in basic environment (NaOH). The functional nanostructures were prepared by using different surfactants (Span80 (span) and a mixture of Igepal co-630 and Brij52 (mix)) to optimise the ME stability and hydroxides biocompatibility as well as to tune the droplets sizes. X-ray Diffraction (XRD) analyses testify the achievement of pure brucite-$Mg(OH)_2$-phase and pure portlandite- $Ca(OH)_2$-phase with a high degree of crystallinity. Besides structural characterisations, the products were thoroughly characterised by means of several and complementary techniques (Dynamic Light Scattering (DLS), X-ray Photoelectron Spectroscopy (XPS), Scanning Electron Microscopy (SEM), Thermogravimetric Analysis (TGA) and Differential Scanning Calorimetry (DSC), Micro-Raman spectroscopy, Inductively Coupled Plasma Mass Spectrometry (ICP-MS) and Fourier Transform Infrared spectroscopy (FT-IR)) to assess their chemico-physical properties as well as their morphological and microstructural features. The stoichiometry of the doped systems was confirmed by ICP-MS measurements. Finally, the cytotoxicity of nanoparticles was assessed by in-vitro tests using ES2 cells in order to provide preliminary data about the biocompatibility of this kind of nanoparticles. The luminescence of the Eu-doped and Tb-doped materials is clearly visible to the naked eye in the red and green regions, respectively, corroborating their employment as materials for imaging in the optical window of interest.

Introduction

In the last years, bioimaging and drug delivery based on nanostructures (i.e. nanoparticles, vesicles, dendrimers, etc) have gained an impressing interest, as witnessed by several studies and patents.[1-4] As a matter of fact, if these nanostructures are suitably functionalised with fluorescent organic dyes or doped with luminescent ions, they can be used for molecular bioimaging. For instance, polymeric NPs functionalised with organic dyes find several applications in targeting and imaging in living cells.[5] As inorganic alternative to organic fluorophores, quantum dots (QDs), semiconductor and metal NPs have also been intensively studied for these applications.[6] Although QDs display good luminescent properties and a greater chemical and photochemical stability compared with organic dyes, they are usually based on toxic metals (i.e. Cd, Pb) which strongly decrease their biocompatibility and limit their possible use in nanomedicine.[7] As far as metal NPs, such as for instance Au NPs, are concerned, their optical and magnetic properties make them suitable for imaging, targeting and photothermal therapy but cytotoxicity is still topic of debate.[8-10]

At variance to the just mentioned NPs, those based on Mg and Ca oxide, hydroxide, phosphate and carbonate are particularly appealing for their higher biocompatibility and stability in cellular environment.[11-14] Furthermore, due to the chemical nature of their surface, they can be easily functionalised with molecules endowing them with lock-and-key binding specificity and they can be easily doped with lanthanides (Ln) ions which confer them luminescent properties.[15-17] As far as calcium and magnesium hydroxides are concerned, they are currently extensively used in biomedical applications: magnesium hydroxide is used for instance as antacid in stomach diseases, calcium hydroxide for

[a] *Dipartimento di Scienze Chimiche, Università degli Studi di Padova, via Marzolo, 1, I-35131, Padova, Italy*
E-mail: silvia.gross@unipd.it
[b] *Istituto per l'Energetica e le Interfasi, IENI-CNR and INSTM, UdR, via Marzolo, 1, I-35131, Padova, Italy*
[c] *Dipartimento di Biotecnologie, Università degli Studi di Verona, Strada Le Grazie 15, 37314 Verona, Italy and INSTM, UdR Verona*
[d] *University of Trento, Department of Industrial Engineering and BIOtech Research Center, Trento, Italy; European Institute of Excellence on Tissue Engineering and Regenerative Medicine, Trento, Italy*
† *Electronic Supplementary Information (ESI) available: Figures E.S.I. 1-5. See DOI: 10.1039/b000000x/*

endodontic therapy.[18, 19] Despite these features make Ln-doped Mg and Ca hydroxides potential candidates for application as contrast agents for bioimaging, they have not yet been used, to the best of our knowledge, for this purpose. In the literature, only reports on luminescent layered double hydroxide[20] and on rare-earth doped or rare-earth based nanoparticles[21] are extensively reported, but no study on rare-earth doped magnesium and calcium hydroxide has been reported yet. These hydroxide systems can be addressed either by solid state or by wet chemistry approaches. Among the latter, the MEs one is particularly appealing being an easy, fast, reproducible and cost effective method. Particularly, it is mostly exploited for the syntheses of polymeric[22-24] and hybrid NPs, whereas it was less intensively used for crystallisation of inorganic systems.[25-28] Nevertheless, it has recently been assessed the effectiveness of the inverse ME for the synthesis of different inorganic systems, ranging from pure and doped ZnO,[29, 30] to iron oxide, calcium carbonate, zirconium dioxide [31], lanthanides oxides,[32] titania,[33] silica, ceria,[27] hydrous zirconia and hafnia.[34, 35] In this regard, it is noteworthy that Muñoz-Espì et al. have recently described progresses in the achievements of crystalline inorganic nanostructures by ME without the need of any subsequent thermal treatment.[27, 28] ME droplets act as nanoreactors, thus enabling to perform the desired precipitation in a confined space, with a good control over the material final size and crystallinity. Furthermore, MEs allow an easy route to functionalise the surface of the NPs by ligand exchange methods or post-reaction functionalisation for nanomedicine applications. Incidentally, MEs, or nanoemulsions, have already found application in nanomedicine,[36-38] and have for example been investigated for human trial of intranasal vaccines.

In this study we addressed the controlled growth of lanthanide-doped $Mg(OH)_2$ and $Ca(OH)_2$ NPs to be used as luminescent contrast agent in bioimaging applications. More specifically, we optimised a fast, easy, low temperature and cost effective method for the ME based synthesis of pure and doped magnesium and calcium hydroxides in confined space. Furthermore, the synthesis was complemented by a thorough chemico-physical characterisation of the products, as well as by a functional assessments in terms of i) optical properties of the doped nanostructures, ii) stability in physiological conditions and iii) cytotoxicity behaviour in view of the application of these NPs as contrast agents for both in-vitro and in-vivo bioimaging.

Experimental Section

Chemicals

Magnesium nitrate hexahydrate ($Mg(NO_3)_2{\cdot}6H_2O$), europium (III) nitrate pentahydrate ($Eu(NO_3)_3{\cdot}5H_2O$), terbium (III) nitrate hexahydrate ($Tb(NO_3)_3{\cdot}5H_2O$), sodium hydroxide (NaOH), Igepal co-630 ($(C_2H_4O)_n{\cdot}C_{15}H_{24}O$, n=9-10), Brij 52 ($C_{16}H_{33}(OCH_2CH_2)_nOH$, n~2), Span 80 ($C_{24}H_{44}O_6$) and cyclohexane ($C_6H_{12}$) were purchased from Aldrich, Milan, Italy. Samarium (III) acetate hydrate ($C_6H_9O_6Sm{\cdot}H_2O$) was obtained from Strem chemicals, Newburyport, Massachusetts. Calcium nitrate tetrahydrate ($Ca(NO_3)_2{\cdot}4H_2O$) was purchased from Carlo Erba Reagenti, Milan, Italy. All chemicals were used without further purification.

Nanoparticles synthesis

$Mg(OH)_2$ nanoparticles (NPs) were synthesised by miniemulsion (ME) technique using two different surfactant systems (Span 80 (span) and a mixture of Brij52:Igepal co-630 (mix), weight ratio 3:1 (3:1 mix)), whereas $Ca(OH)_2$ NPs were obtained only with the mixture of Brij52:Igepal co-630 3:1.

For NPs synthesised by using the mix, two identical suspensions were prepared by dispersing the surfactant mixture (0.8 g) in cyclohexane (8 g). Then an aqueous 0.5 M solution of $Mg(NO_3)_2{\cdot}6H_2O$ (3 mL, 1.5 mmol) were added to mixture A and an aqueous 1 M solution of NaOH (3 mL, 3 mmol) to mixture B, to get a Mg:NaOH molar ratio of 1:2. Both emulsions were then separately sonicated for 3 minutes, by using a Sartorious Stedim LabsonicP homogeniser, mounting a 3 mm titanium tip and operating at amplitude of 70%, corresponding to an acoustic power of 322 Wcm^{-2}, giving MEs A' and B', respectively. These MEs were then mixed, stirred and sonicated again for 3' thus yielding ME C. The same method was used for the synthesis of $Ca(OH)_2$ NPs. A schematic representation of the synthesis procedure is reported in Scheme 1.

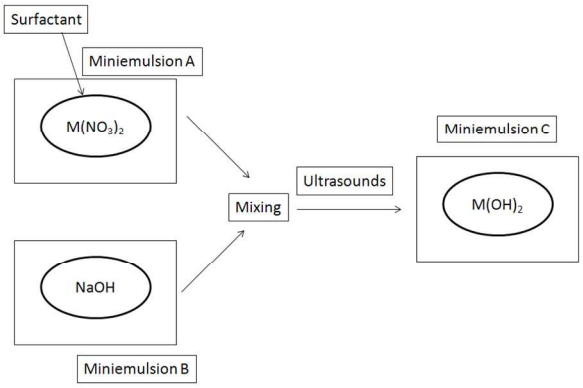

Scheme 1 Schematic representation of the synthesis procedure

The procedure for synthesising NPs with Span 80 was the same, although different concentrations, due to the different HLB value of the surfactant, were used. Indeed MEs A and B were prepared by dispersing Span 80 (0.75 g) in cyclohexane (24 g). Then, an aqueous solution of $Mg(NO_3)_2{\cdot}6H_2O$ 0.5 M (6 ml, 3 mmol) and an aqueous solution of NaOH 1 M (6 ml 6 mmol) (molar ratio Mg:OH 1:2) were added to ME A and ME B, respectively, using the amount of substances reported by Landfester *et al.*[39] Subsequently the two MEs were mixed, stirred and sonicated for 3'as in the previous case. In both cases ME C were allowed to stand overnight. The white precipitate formed was separated by centrifugation (10000 rpm for 10 minutes) and washed 3 times with deionised water and, in the case of Span 80 ME, also with ethanol. For the preparation of lanthanides doped $Mg(OH)_2$ and $Ca(OH)_2$,an appropriate amount of Eu^{III}, Sm^{III} or Tb^{III} was added at mixture A to achieve the atomic ratios Mg/Ca:M (M=Eu, Sm, Tb) of 20:1 and then the procedure described above was carried out.

Characterisation methods

DLS analysis

DLS analyses on the as-prepared suspensions were carried out using a Malvern ZetasizerNano S, at a temperature of 20 °C.

FT-IR analysis

FT-IR and FT-IR/ATR experiments were performed with a NEXUS 870 FT-IR (NICOLET), operating in the transmission range 4000-400 cm^{-1}, collecting 64 scans with a spectral resolution of 4 cm^{-1}. The measurements were recorded by dispersing the powders in anhydrous KBr.

Thermogravimetric analysis

The thermogravimetric analyses (TGA) were performed in air on a LabSysSetarm SDT 2960 instrument in the temperature range 20-800 ° C using a heating rate of 10° C min^{-1}.

Raman analysis

Raman experiments were performed with a Thermo Scientific DXR Raman microscope operating in the range 100-6000 cm^{-1}, with a solid state laser of wavelength equal to 532 nm^{-1} and a 10x objective. All spectra were normalised to 1 before plotting them.

Scanning Electron Microscopy

Measurements were performed using a Field Emission (FE-SEM) Zeiss SUPRA 40VP (Dipartimento di Scienze Chimiche, Università di Padova, Italy), with a primary beam acceleration voltage of 3 kV and a conventional secondary electron detector for the SEM investigations.

XPS analysis

The powders were investigated by XPS with a Perkin-Elmer Φ 5600ci instrument using standard Al-K_α radiation (1486.6 eV) operating at 350 W. The working pressure was $<5\cdot10^{-8}$ Pa $\sim10^{-11}$torr. The calibration was based on the binding energy (BE) of the $Au4f_{7/2}$ line at 83.9 eV with respect to the Fermi level. The standard deviation for the BE values was 0.15 eV. The reported BE's were corrected for the BE's charging effects, assigning the BE value of 284.6 eV to the C1s line of carbon.[40] Survey scans were obtained in the 0 - 1350 eV range (pass energy 187.5 eV, 1.0 eV/step, 25 ms/step). Detailed scans (29.35 eV pass energy, 0.1 eV/step, 50-150 ms/step) were recorded for the O1s, C1s, Mg2s, Mg1s, Mg 2p, Mg KLL, Ca2p, Ca2s, Eu3d, Sm3d, Sm4d, Tb3d and 4d regions. The atomic composition, after a Shirley-type[41] background subtraction was evaluated using sensitivity factors supplied by Perkin-Elmer.[42] Charge effects were partially compensated by using a charge neutraliser (flood gun). Peak assignment was carried out according to literature data.

X-Ray diffraction

XRD data was collected with a Bruker D8 Advance diffractometer equipped with a Göbel mirror and employing the CuK_α (λ = 0.15405 nm) radiation. The angular accuracy was 0.001° and the angular resolution was better than 0.01°. All patterns were recorded in the range 10-80° with a scan step of 0.03 (2θ) and a 7 secs/step acquisition interval.

ICP-MS (Chemicals and procedure)

All reagents were of analytical grade and were used as purchased: HNO_3 (CAS Number 7697-37-2) 70%, purified by redistillation, ≥99.999% (Sigma Aldrich), $HClO_4$ 70% RP Normapur (Prolabo, France). Ca (1000 mg/l) and Mg (10 mg/l) were present in the multi-element standard Solution CPAchem ICP-MS Calibration Standard Ref N: MS19EB.10.2N.L1. Eu, Sm and Tb (all 1 mg/l) were present in the ICP-MS Calibration Standard Ref N: MS98B2.1.2N.L1. All solutions were prepared in milliQ ultrapure water obtained with a Millipore Plus System (Milan, Italy, resistivity 18.2 Mohm cm^{-1}). The ICP-MS was tuned daily using a 1µg/l tuning solution containing ^{140}Ce, ^{7}Li, ^{205}Tl and ^{89}Y (Agilent Technologies, UK). A 100 µg/l solution of ^{45}Sc and ^{115}In (Aristar®, BDH, UK) prepared in 2% (v/v) nitric acid was used as an internal standard through addition to the sample solution via a T-junction.

ICP-MS (Solution setup)

Multi element standard solutions were prepared in 2% v/v HNO_3. The calibration solutions were prepared by gravimetric serial dilution from multi-element standard solutions, at six different concentrations (min. 10 ppb–max. 1000 ppb). Calibration plots were obtained with an internal standard. In particular, Ca and Mg refer to the ^{45}Sc internal standard; Eu, Sm and Tb refer to the ^{115}In internal standard. All regressions were linear with a determination coefficient larger than 0.9999. To check for instrumental drift, one of the multi-element standards was analyzed every 10 samples. The internal standard concentration of both In and Sc was 100 ppb in all samples and blanks. Blank samples of ultrapure water and reagents were also prepared using the same procedures as for the samples. All blank levels obtained were subtracted appropriately.

ICP-MS (NPs digestion)

NPs doped samples (50 mg) were placed in a 25 ml digestion vials and added with 3 ml of 70% HNO_3 and 3 ml 60% $HClO_4$. Vials were heated on a hot plate at 200 ± 10 °C for 150 min. A PTFE cap was used to minimise sample loss from the vial. Vials were then cooled and the obtained solution was diluted with 2% v/v HNO_3.

All the elements were measured by using inductively coupled plasma coupled to a mass spectrometer (ICP-MS) Agilent Technologies 7700x ICP-MS system (Agilent Technologies International Japan, Ltd., Tokyo, Japan), equipped with an octupole collision cell operated in kinetic energy discrimination mode. The instrument was optimised daily to achieve optimum sensitivity and stability according to manufacturer recommendations. Typical operating conditions and data acquisition parameters are summarised in Table 1. All parameters were checked daily using an in-house optimisation program.

Table 1 Instrumental operation conditions for ICP-MS

Instrumental	Agilent 7700x ICP-MS
RF power	1550 W
RF matching	1.8 V
Plasma gas flow rate	15 l min−1 Ar
Auxiliary gas flow rate	1.0 l min−1 Ar
Carrier gas flow rate	1.05 l min−1 Ar
Make-up gas flow rate	0.0 l min−1 Ar
He gas flow	4.3 ml/min
CeO+/Ce+	0.902%
Ratio(2+) 70/140	0.944%
Nebulizer	Microflow PFA nebulizer
Spray chamber	Scott double-pass type at 2 °C
Torch	Quartz glass torch
Sample uptake rate	0.1 ml min−1
Sample cone Nickel	1.0 mm aperture i.d.
Skimmer cone Nickel	0.5 mm aperture i.d.
Sampling depth	8.5 mm
Detector mode	Dual (pulse and analog counting)

Photoluminescence measurements

Luminescence measurements were performed using a tunable dye laser pumped by a Nd:YAG laser as the excitation source. The emission signal was analyzed by a half-meter monochromator (HR460, JobinYvon) equipped with a 150 or 1200 lines/mm grating and detected with a CCD detector (Spectrum One,

JobinYvon) or with a photomultiplier. The spectral resolution of the emission spectrum is about 0.2 nm. The emission decay curves were recorded upon pulsed laser excitation and detected with a GaAs photomultiplier (Hamamatsu) and a 500 MHz digital oscilloscope (WaveRunner, LeCroy).

Leaching and stability tests

A known amount of the NPs powders (about 1 mg) was dispersed in 1 ml of solvent (either MilliQ, PBS or acidulated PBS, at pH=5.5) and stored in the given solvent at 37°C for 1 week. After this time, the suspensions were centrifuged and 0.5 ml of the surnatant was collected and diluted with HNO_3 5% w/w solution to a total mass of 3 ml. The obtained solutions were subsequently analysed by ICP-MS.

Cell culture

Human ovarian carcinoma cells ES2 were cultured in T75 flasks until confluence in RPMI-1860 (Euroclone, Italy) supplemented with 10% inactivated fetal bovine serum, 2 mM L-Glutamine and penicillin-streptomycin (Invitrogen, US). Then, cells were trypsinised and seeded in 48-well plates at a density of $2 \cdot 10^4$ cells/cm^2 in 1 ml of medium. 24 hours after seeding, cells started to be cultured in full medium with Ca_mix or Mg_mix NPs, Mg_span, or Mg_Eu_mix and Mg_Sm_mix NPs. Two concentrations were chosen to evaluate the influence of each NP on cell behaviour: 100 µg/ml (high concentration) and 30 µg/ml (low concentration). As a negative control for the following tests, a group of samples were kept in NP-free medium.

Before use, NPs were incubated in ethanol 70% (Roth, Germany) overnight at 4°C. Subsequently, after a centrifugation for 5 minutes at 3000 rpm, NP were resuspended in sterile distilled water and centrifuged again three times to completely remove the ethanol. After the last centrifugation, NPs were dispersed in full media at the appropriate concentrations.

AlamarBlue assay

Cell viability was evaluated after 2, 24 and 48 hours of incubation in medium with NPs. To this purpose, AlamarBlue assay (Invitrogen, US) was performed according to manufacturer's instructions. Briefly, culture medium (with or without NP) was removed from samples and substituted with 1 ml of full medium with 10% v/v of AlamarBlue solution. Cells were incubated at 37°C for 3 hours and subsequently, 100 µl of the supernatant were transferred in a black 96-well plate. The amount of AlamarBlue reduced by viable cells was assessed measuring the corresponding fluorescence signal (excitation wavelength: 565 nm; emission wavelength: 595 nm) with a micro plate reader (Tecan Infinite M200 Pro). 10% v/v AlamarBlue solution was also incubated as a control and its fluorescence was subtracted from those of samples.

Lactate dehydrogenase assay

Cytotoxicity of $Ca(OH)_2$ and $Mg(OH)_2$ NPs at high and low concentration was evaluated after 24 hours of incubation. A lactate dehydrogenase-based (LDH) assay was used (*in vitro* toxicology assay kit, Sigma-Aldrich, US) following the provided instructions. In short, LDH enzymes are released by cells into the external environment when the cellular membrane is damaged. Therefore, the activity of LDH in the culture medium is a measure of cell necrosis and/or apoptosis and can be evaluated by means of a colorimetric reaction involving the reduction of NAD and the subsequent conversion of a tetrazolium salt into a coloured compound. The amount of this product after the enzymatic reaction in the sample culture media was assessed measuring the absorbance of the supernatant at 490 nm, using the absorbance at 690 nm as a reference to normalise the measurements.

Statistical analysis

Each test was performed on N = 3 independent determinations per data point. Results are presented as mean ± standard error and were subjected to one-way or two-way ANOVA with Tukey post-test. Before applying the tests, the equality of variances was verified. All statistical analyses were performed using GraphPad Prism 4.0 (GraphPad software, US). Significance was assigned at p-values less than 0.05.

Results and Discussion

As extensively described in the Experimental Section, the final ME was achieved by sonication of the two precursors MEs (one containing the metal salt and the other NaOH as precipitating agent), thus affording the precipitation of the hydroxides in the nanodroplets produced by ultrasound shear forces. Immediately after the sonication, the average hydrodynamic diameter of w/o droplets was investigated by Dynamic Light Scattering (DLS). In the case of MEs prepared with Span 80, the average hydrodynamic diameter always resulted to be ~130 nm (Table 2 and Fig. E.S.I 1), with a good reproducibility. Analogous results were found for lanthanide doped NPs. At variance, the average hydrodynamic diameter of both MEs prepared with the mix for $Mg(OH)_2$ (Mg_mix) and $Ca(OH)_2$ (Ca_mix) NPs, was not completely reproducible, and with a much greater average value. A tentative explanation of such a finding could be the different distribution in suspension of Igepal CO-630 and Brij52 which thus generate a polydispersed suspension.

Table 2 Average droplet hydrodynamic diameter, as determined by DLS

Sample	Average diameter (nm)
Mg_span	130
Mg_mix	430
Ca_mix	460

Once separated the powder from the suspension, the crystallographic structure and the average NPs crystallite size were obtained by XRD analyses (see Figure 1and Table 3).

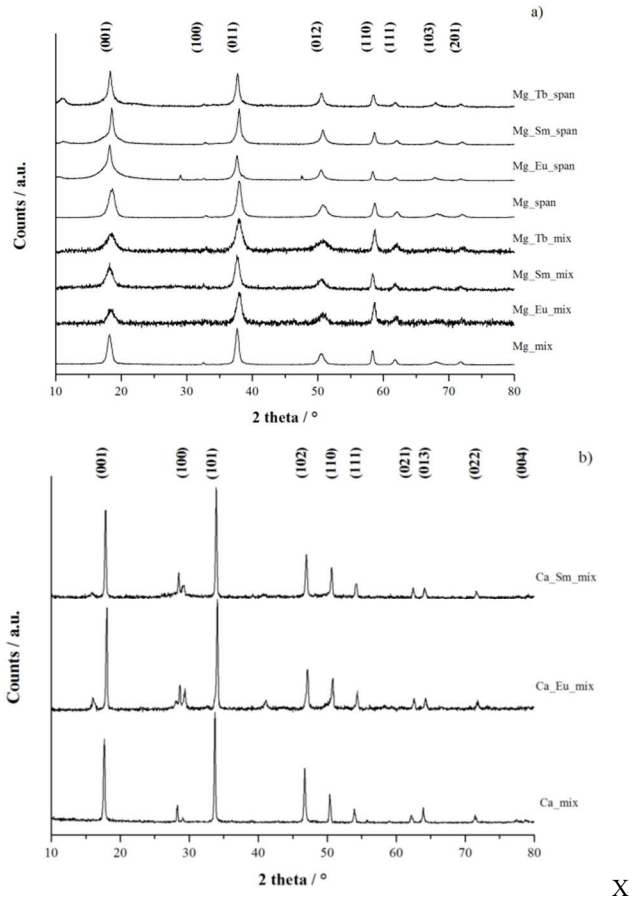

Fig. 1 XRD diffractograms of pure and doped $Mg(OH)_2$ (a) and $Ca(OH)_2$ (b)

Independently from the used surfactant, the crystallographic structure of $Mg(OH)_2$, both pure and doped, was *brucite* (Powder Diffraction File, PDF: 01-083-0114) while the crystallite size, calculated with the Scherrer equation,[43] was for both class of systems ~20 nm. In $Ca(OH)_2$ NPs, characterised by the *portlandite* structure (PDF: 00-001-1079), the average size, for both pure and doped NPs, was about 35 nm. Calcium hydroxide X-ray powder patterns of both pure as well as doped systems and Mg_Eu_span are characterised by the presence of further phases. These phases are due to the formation of crystalline $Eu(OH)_3$ (PDF: 01-083-2305) in Ca_Eu_mix NPs, and of $Sm(OH)_3$ (PDF: 01-083-2036) in Ca_Sm_mix. As for Mg_Eu_span, the diffractograms present additional features that are most probably due to small traces of residual starting reagents. The XRD reported results prove the effective formation of a crystalline phase even at room temperature (RT) and without the need of subsequent thermal treatments. Furthermore, these results are consistent with a good reproducibility of the crystalline phase and of the average crystallite dimensions. It should be underlined that this data has not to be compared with this retrieved by DLS, since the former is referred to the average crystallite size, the latter to the hydrodynamic diameter, including the surfactant shell.

Table 3a Crystallographic data of brucite $Mg(OH)_2$ and $Ca(OH)_2$ hexagonal P-3m1

	$Mg(OH)_2$	$Ca(OH)_2$
Lattice parameters (PDF) [Å]	a=b=3.1477, c=4.7717	a=b=3.5890, c=4.9110
Volume (CD) (PDF) [Å^3]	40.94	54.78
Ionic radius (Mg^{II}/Ca^{II}) [pm]$^{a)}$	72	100

Table 3b Average crystallite size of brucite $Mg(OH)_2$ and $Ca(OH)_2$

Sample	Scherrer [nm]	Crystallographic phase
Ca_mix	40	Portlandite
Ca_Eu_mix	36	Portlandite
Ca_Sm_mix	38	Portlandite
Mg_mix	15	Brucite
Mg_Eu_mix	12	Brucite
Mg_Sm_mix	11	Brucite
Mg_ mix	8	Brucite
Mg_span	11	Brucite
Mg_Eu_span	20	Brucite
Mg_Sm_span	21	Brucite
Mg_Tb_span	12	Brucite

In order to evaluate the influence of the different surfactants on the nanostructures morphology, SEM micrographs were accordingly registered. In Figure 2a, the micrograph for Mg_mix is exemplarily reported and it evidences the presence of aggregates of flake-like nanostructures. Conversely, the morphology of Ca_mix (Figure 2b) is less defined, but in these case there is a tendency to form spherical particles, which easily agglomerate; a similar spherical morphology is detected also for Ca_span (see Figure E.S.I. 2). These results indicate that for these systems the morphology is strongly dictated by the nature of the compounds, whereas the surfactants play only a minor role. The sizes of the structures evidenced by SEM are much larger than the crystallite sized obtained by XRD, but are in agreement with droplet diameters determined by DLS. These findings hint at the aggregation on the smaller crystallites within the droplet compartments.

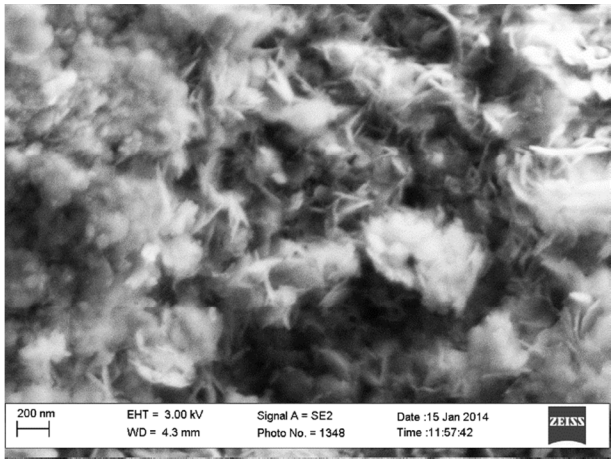

a)

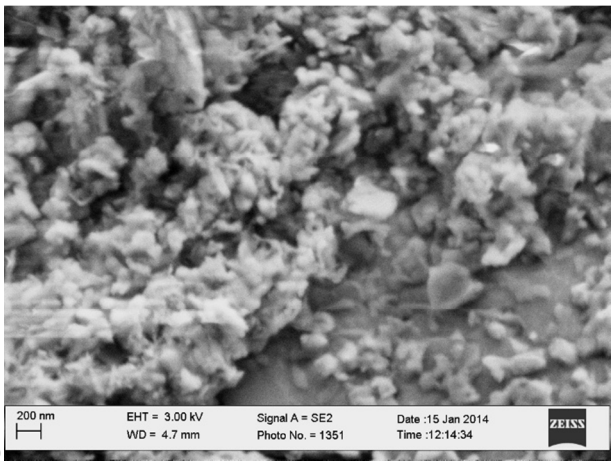

b)

Fig. 2 SEM micrographs of Mg_mix (a) and Ca_mix (b)

Since it is the surface of these systems which is expected to interact with the cellular environment in biological applications, the surface composition and the oxidation state of surface species were investigated by means of XPS measurements. In Figure 3, the survey spectra of Mg_Sm_mix and Ca_Sm_mix are displayed. Detailed scans were recorded for the regions of interest, as reported in the Experimental Section, to obtain more accurate binding energy (BE) values and to perform the quantitative analysis (see Table 4).

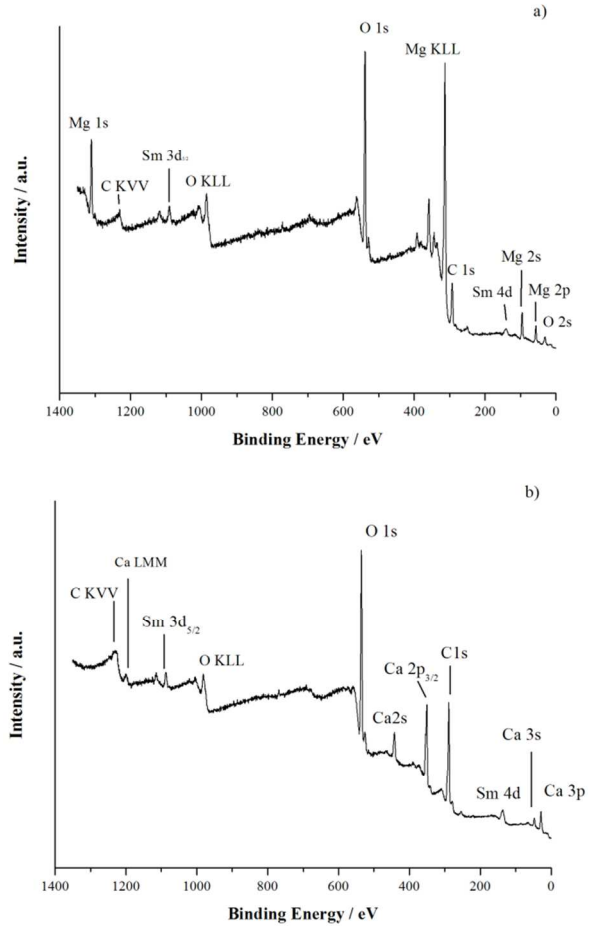

Fig. 3 XPS survey spectra of Mg_Sm_mix (a) and Ca_Sm_mix (b) (graphs shown are not corrected for surface charging effects)

Table 4 XPS BE values and quantitative data. Values of BE were corrected considering charging effects

BE [eV]	C1s	O1s	Mg 2p/Ca2p$_{3/2}$	Dopant	% C	% O	% Mg/ Ca	% Sm
Mg_Sm_mix	284.6 285.5 286.3	530.3	49.7	Sm3d$_{5//2}$ 1083.2	56.3	31.6	11.4	0.7
Ca_Sm_mix	284.6 285.8 288.7	530.9	346.7	Sm3d$_{5/2}$ 1083.0	66.3	24.3	8.8	0.6

The high carbon and oxygen percentages detected on the surface of all the systems are reasonably ascribed to the presence of the surfactant on the NPs surface, particularly carbon derived from the aliphatic chain and oxygen from the polar head of these molecules. With specific reference to the carbon C1s spectrum (see Figure 4), a contribution at 284.6 eV due to alkyl groups and, partially, to external contamination is always present. A further contribution due to surfactants aliphatic chains is detected at 285.5 eV, whereas contribution due to polar chains (C-O-C, C-OH) is, according to literature, peaked at 286.7 eV, for all the samples.[44-46]

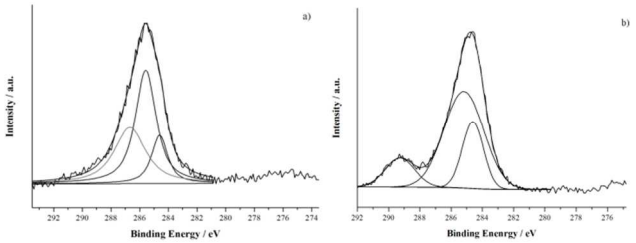

Fig. 4 C1s peak of Mg_Sm_mix (a) and Ca_Sm_mix (b) (graphs shown are corrected for surface charging effects)

The presence of the surfactant was also confirmed by FT-IR and TGA data (vide infra). The comparison of BEs with literature data indicates that Ca2p$_{3/2}$, Mg1s and Mg2s regions have the typical binding energy values of calcium and magnesium hydroxides, as shown in Table 4.[47, 48] In these samples, Mg 2p is found at 49.7 eV, i. e. the typical value for $Mg(OH)_2$,[42, 49, 50] whereas Ca2p$_{3/2}$ is found at 346.7 eV which is a typical value for $Ca(OH)_2$.[42, 48-51] Due to the low atomic concentrations involved, Mg/Ca_Sm_mix samples are the only two for which the dopant is clearly visible. The BE value for Sm 3d$_{5/2}$ (1083.0 eV) confirms the presence of samarium in oxidic environment.[42, 47, 48]

To accurately assess the actual atomic ratios in the doped systems, ICP-MS measurements were carried out. Expected and found stoichiometric atomic ratios for calcium and magnesium and the doping elements (Eu, Sm and Tb) are reported in Table 5. Experimental evidences herein reported statistically coincide with the expected values for all but one (Mg_Ln_span) sample series, for which the Mg:Ln ratios in Mg_Ln_span are larger than the expected ones. Since the Mg amount is in agreement with nominal values, these samples are likely characterised by a lanthanides leakage. As a whole, ICP results highlight the effectiveness of the adopted synthetic route to accurately control the stoichiometry and the actual doping level of final products.

Table 5 Calculated (second column) and experimental (third column) atomic ratios between Mg and Ca with the doping elements (Eu, Sm and Tb), as determined by ICP-MS. The used surfactants are reported in the last column.

Sample	Calculated atomic ratio	Experimental atomic ratio	Surfactant
Mg_Eu_mix	20	19±2	Mix
Mg_Sm_mix	20	22±3	Mix
Mg_Tb_mix	20	19±3	Mix
Mg_Eu_mix	100	97±6	Mix
Mg_Eu_span	20	209±13	Span 80
Mg_Sm_span	20	303±20	Span 80
Mg_Tb_span	20	96±5	Span 80
Ca_Eu_mix	20	16±5	Mix
Ca_Sm_mix	20	16±5	Mix

The expected presence of the surfactant on the NPs surface was confirmed by FT-IR spectra recorded for pure Mg_mix, Ca_mix NPs and for pure Mg_span NPs. In the first two cases, vibrational bands are observed at 3700 and 3400 cm^{-1}. These bands are straightforwardly ascribed to the stretching of –OH groups, particularly of free –OH (the sharp one at higher wavenumbers), and of H-bonded hydroxyl groups (the broad one at lower wavenumbers), which are assignable to the surfactant and the hydroxides, respectively. Further bands characteristic of surfactants are those at 2920 and 2850 cm^{-1} (ν CH_2), at 1645, 1520, 1260 cm^{-1} (ν (C=C) aromatic and δ (=C-H)) typical of Igepal co-630. In the Ca_mix case, the two further bands at 875 and 785 cm^{-1} are characteristic of aromatic out-of-plane deformations. Finally bands at about 1100 cm^{-1} and 1020 cm^{-1} are due to C-O-C vibration of ether moieties of Brij 52.[52] Spectra are shown in Figure E.S.I. 3a, b. FT-IR Attenuated Total Reflectance (ATR) spectra of pure surfactants are also reported in SI (Figure E.S.I. 3).

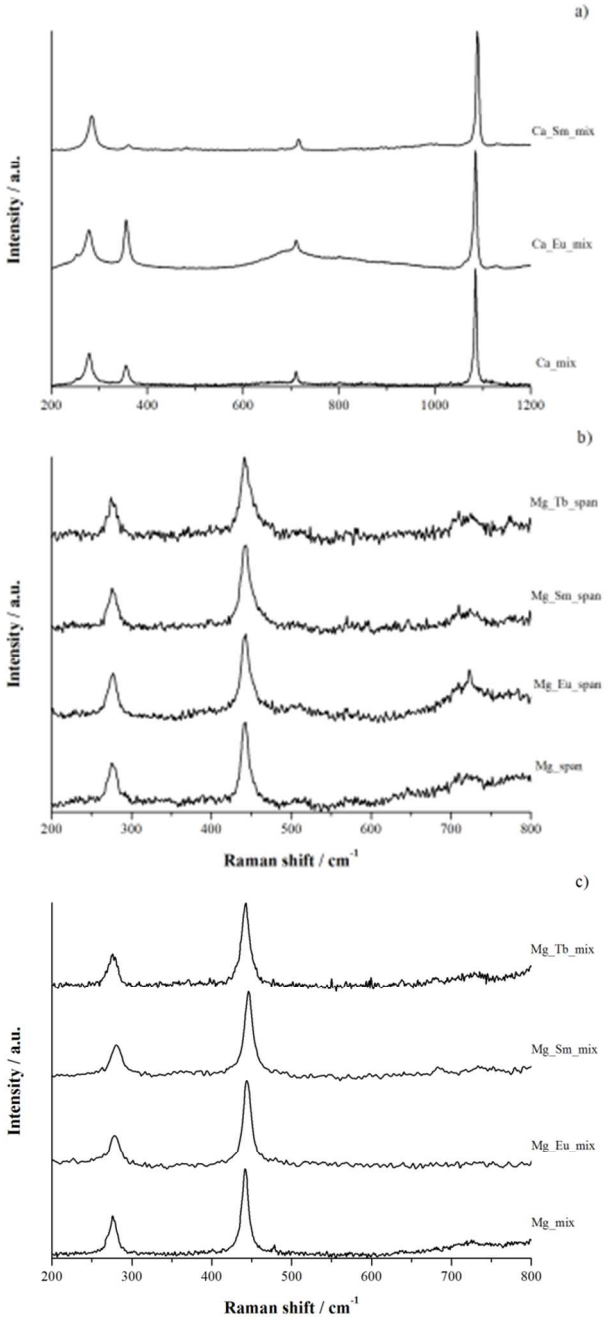

Fig. 5 Normalised Raman spectra of: a) pure and doped Ca_mix, b) pure and doped Mg_span, c) Mg_mix samples

A further hint on the composition of the prepared samples was provided by Micro-Raman analyses. This technique is indeed extensively used for the analysis of nanostructured materials, since it allows to analyse their composition, the presence and nature of crystalline phases contemporary present as well as the domain dimensions.[53, 54] Spectra recorded for pure and doped Ca_mix NPs show the presence of characteristic peaks of portlandite-calcium hydroxide, particularly of the Ca-O stretching (253 cm^{-1}, 355 cm^{-1}) as shown in Figure 5. Further peaks at higher Raman shifts are ascribed to the surfactants used in these synthesis (Igepal co630 and Brij 52), whose spectra are reported in Figure E.S.I. 4. These samples show evidence of carbonations

and characteristic peaks of aragonite $CaCO_3$ at 278, 711 and 1085 cm^{-1} are present in all the spectra.[55-59] Pure and doped $Mg(OH)_2$ samples, obtained using both Span 80 and the surfactant mix show typical brucite Mg-O vibration peaks in $Mg(OH)_2$ at 275, 442 and 721 cm^{-1}.[60, 61] Other peaks are ascribed to Span 80, Igepal CO-630 and Brij 52 (Figure E.S.I. 4).

To evaluate quantitatively the amount residual surfactant on NPs, TGA-DSC analyses were also carried out on Mg_mix (Figure 6). In the range up to 200 °C, a weight loss of ~ 3%, due to the release of physisorbed water was revealed. Above this temperature and up to ~ 340°C another weight loss of ~ 7% takes place, which is associated to the decomposition of the two surfactant molecules (Igepal co-630 and Brij 52). This is confirmed by the exothermic peak at 305 °C, observed in the DSC trace, and by the comparison with the thermogravimetric curves recorded for the pure surfactants (Figure E.S.I. 5). In the temperatures range 340-400°C a further weight loss of about 27%, due to the dehydration of $Mg(OH)_2$, according to equation (1) and confirmed by the endothermic peak at 387 °C, is detected. This weight loss is in agreement with the final residual weight.[62]

$$Mg(OH)_2 + 84.5\ kJ/mol \rightarrow MgO + H_2O \qquad (1)$$

Cytotoxicity tests and luminescence measurements were performed to assess the suitability of our products for bioimaging applications.

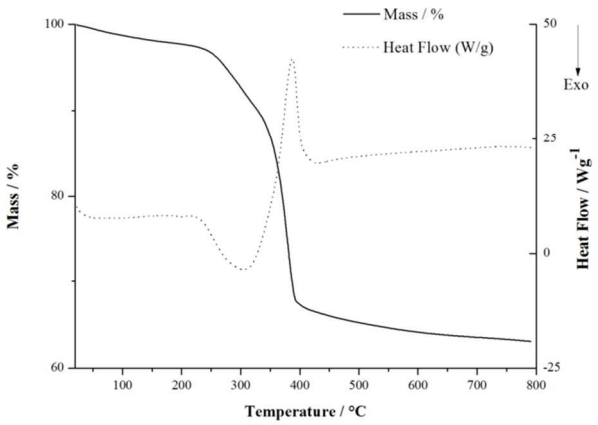

Fig. 6 TGA-DSC curve of Mg_mix NPs

Ovarian carcinoma cells (ES2 cells) were used as an *in vitro* model and incubated with NPs at two different concentrations (100 μg/ml and 30 μg/ml). Cell viability was monitored through the Alamar Blue assay, while the LDH (lactate dehydrogenase)-based test was then employed to estimate the possible NPs induced cell death after 24 hours of culture. Results for $Mg(OH)_2$ NPs are shown in Figure 7: Fig. 7A refers to the cytotoxicity measurements for Mg_mix, Mg_span and Mg_Eu_mix, respectively. The absorbance values are proportional to the amount of the LDH enzyme released by dead cells exposed to a high or low concentration of NPs. Cells cultured with NP-free full medium were used as a control. The absence of any significant difference between the absorbance of samples cultured with or without NPs, regardless of the NPs concentration, ultimately testifies that $Mg(OH)_2$ NPs are not cytotoxic at the used concentrations. Moreover, neither the employed surfactant nor the doping ions influence this evidence. Similar results were also observed when Sm^{III} ions were used to dope $Mg(OH)_2$ NPs (Figure E.S.I. 6). Results pertaining $Ca(OH)_2$ NPs were analogous to those collected for $Mg(OH)_2$: no cytotoxicity at the applied concentrations after 24 hours of culture was revealed (Figure E.S.I. 6).

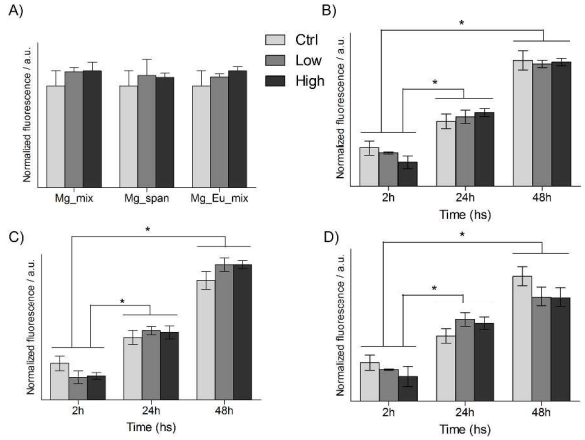

Fig. 7 Results of the LDH-based assay (A) and the AlamarBlue assay (B-D) for Mg_mix (B), Mg_span (C) and Mg_Eu_mix (D) NPs.

A further test to assess the incubated cells viability, based on the Alamar Blue assay, was performed. Figure 7B-D display the results of cell viability measurements after 2, 24 and 48 hours of incubation with $Mg(OH)_2$ NPs at high and low concentrations. At each time point, results are compared with the viability of cells cultured in a NP-free medium, used as blank reference The fluorescence values are proportional to the number of viable cells in the corresponding sample. No differences were detected among pure or Eu^{III} doped Mg_mix, Mg_span NPs: for all samples, regardless of the concentrations used, NPs did not influence cell viability at earlier or later culture times. In fact, cells proliferated significantly after 24 and 48 hours culture and the number of viable cells was comparable among samples cultured with or without NPs. Similar outcomes were obtained for $Mg(OH)_2$ NPs doped with Sm^{III} and for undoped $Ca(OH)_2$ nanostructures (Figure E.S.I. 6). Therefore, doped $Mg(OH)_2$ NPs can be potentially employed in the bioimaging field, since they showed neither cytotoxicity nor influence on cell viability at concentrations lower than 100 μg/ml, regardless of the used surfactant.

The stability of $Mg(OH)_2$ NPs in physiological conditions was evaluated by leaching tests. Eu^{III} doped and undoped $Mg(OH)_2$ nanoparticles were suspended in different aqueous solutions: MilliQ water, 1x PBS (pH=7) and acidulate PBS (pH=5.5) at 37°C for 1 week. Our aim was to verify no relevant leaching of the Mg and particularly of the hazardous lanthanide ions. The results are summarized in Table 6: the leaching is very low, thus assessing the nanostructures as stable in the physiological media. Interestingly, in the physiological conditions (PBS at pH=7), the amount of leached Mg is lower than in the other two cases; the opposite occurs for Eu.

Table 6 Relative amounts of Mg or Eu leached (with respect to the total amount of element present in the starting sample) after 1 week at 37°C, in various media

Sample	Solvent	Leached Mg (%)	Leached Eu (%)
Mg_mix	MilliQ	5.3	-
Mg_mix	PBS	1.5	-
Mg_mix	PBS 5.5	5.5	-
Mg_Eu_mix	MilliQ	5.5	0.6
Mg_Eu_mix	PBS	1.8	0.9
Mg_Eu_mix	PBS 5.5	3.4	0.5

In addition, the doping process with Eu^{III} or Sm^{III} did not influence these outcomes. The possibility to apply these systems in bioimaging applications entails an efficient and stable luminescence. In this regard, RT emission spectra of Mg_Eu_mix, Mg_Eu_span and Ca_Eu_mix powder samples upon laser excitation at 465 nm are shown in Figure 8 in the 550-750 nm wavelength range.

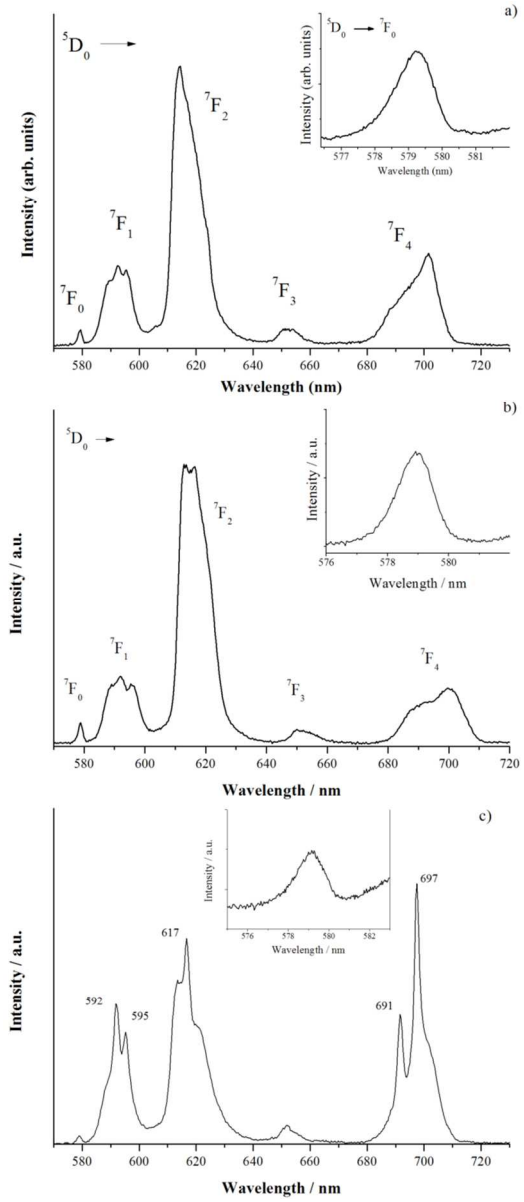

Fig. 8 Room temperature emission spectra of Mg_Eu_mix (a), Mg_Eu_span (b), Ca_Eu_mix (c)

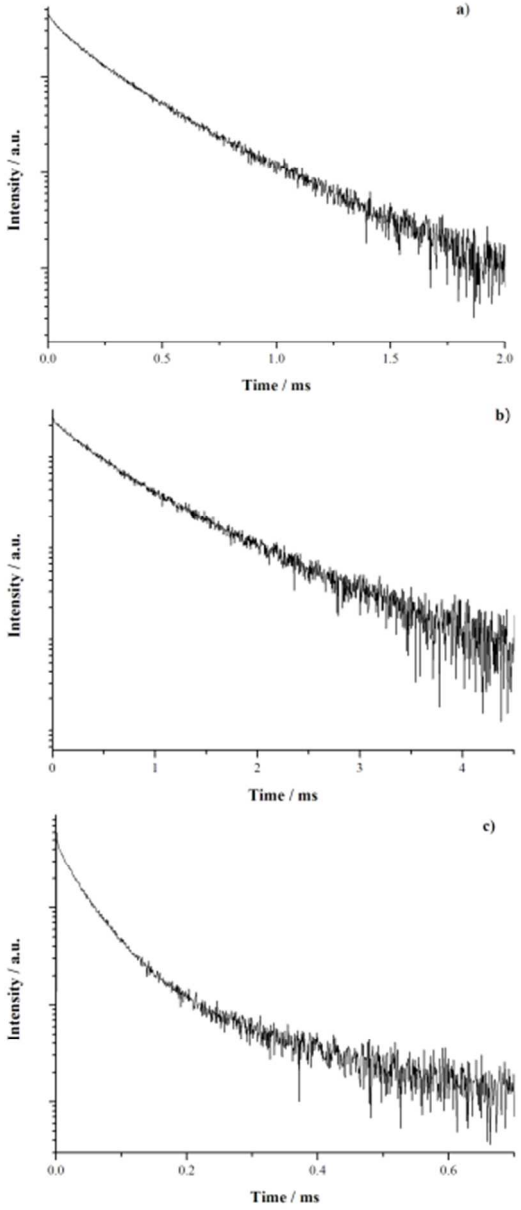

Fig. 9 Room temperature emission decays for Mg_Eu_mix (a), Mg_Eu_span (b), Ca_Eu_mix (c)

The emission bands can be assigned to Eu^{III} $^5D_0 \rightarrow {}^7F_J$ (J=0, 1, 2, 3, 4, see also Figure E.S.I. 7a) transitions (the transitions relative to J=5, 6 should also be mentioned, but, due to their wavelength falling in the IR region, they could not be experimentally detected). For both Eu^{III} doped $Mg(OH)_2$ samples, prepared by using different surfactants, the strongest emission band is peaked at ~ 620 nm, and it is due to the hypersensitive $^5D_0 \rightarrow {}^7F_2$ transition, which clearly dominates the spectra. The allowed $^5D_0 \rightarrow {}^7F_2$ band is stronger than the magnetic dipole $^5D_0 \rightarrow {}^7F_1$ one, suggesting that Eu^{III} ions are located in low symmetry sites, without inversion symmetry. Moreover, the degeneracy of the $^7F_1$ level is completely lifted, since three $^5D_0 \rightarrow {}^7F_1$ bands are clearly visible in the emission spectra, although overlapping each other. This behaviour suggests the presence of a significant broadening

of the emission bands, probably due to structural disorder around Eu^{III} ions, also confirmed by the full width at half maximum (FWHM) of the $^5D_0 \rightarrow {}^7F_0$ (0-0) band, similar to that of Eu^{III} doped glass systems. The Eu^{III} asymmetry ratios R = $I(^5D_0 \rightarrow {}^7F_2)/I(^5D_0 \rightarrow {}^7F_1)$, where I represents the emission integrated intensity of the corresponding band, for the Mg_Eu_span and Mg_Eu_mix samples, result to be 4.36 and 3.84, respectively.[63] These quite high values confirmed the low symmetry of the sites accommodating Eu^{III} ions. On the other hand, the emission spectrum for Ca_Eu_mix sample clearly evidences the presence of europium hydroxide, impurity that is confirmed also by the X-ray diffraction patterns of this sample (see Figure 1b). In fact, some sharp bands, indicated with the wavelength positions, in Figure 8c, are typical of $Eu(OH)_3$, as found by different authors.[64, 65] Nonetheless, from a comparison with the emission spectra reported in the literature, the emission spectrum for the present Ca_Eu_mix sample presents other features which could suggest that some Eu^{III} ions have been incorporated in the calcium hydroxide host. Before going on, it has to be remarked that the Eu^{III} site symmetry in europium hydroxide is relatively low (C_{3h}), explaining the similarity between the emission intensities of the electric dipole allowed $^5D_0 \rightarrow {}^7F_2$ and the magnetic dipole allowed $^5D_0 \rightarrow {}^7F_1$ bands. In the C_{3h} point symmetry, the $^5D_0 \rightarrow {}^7F_0$ band is forbidden, and in fact no such band was observed for europium hydroxide. Therefore, the presence of a weak but clearly visible 0-0 band in the emission spectrum indicates that some Eu^{III} ions are accommodated in sites with lower point symmetries (C_s, C_1, C_n or C_{nv}, n=2, 3, 4, 6) with respect to C_{3h}, according to the electric dipole selection rules for lanthanide ions.[66] It is interesting to note that the point symmetry of calcium ions in calcium hydroxide is D_{3d} and therefore no (0-0) should be observed if Eu^{III} would substitute Ca^{II} ions in the lattice sites. Nonetheless, the presence of distortions of the coordination polyhedron around the Eu^{III} ions or the presence of defects might lift this selection rule and making partially allowed the weak 0-0 band, as observed for the present sample. The emission decays, shown in Figure 9, present a different behaviour for the Eu^{III} doped $Mg(OH)_2$ or $Ca(OH)_2$ samples. In particular, a slightly non-exponential behaviour is observed for the $Mg(OH)_2$ sample, confirming the presence of disorder around the lanthanide ions. The effective decay times, τ_{eff}, was calculated using the equation:[67]

$$\tau_{eff} = \frac{\int tI(t)dt}{\int I(t)dt}$$

In this equation $I(t)$ represents the luminescence intensity at time t corrected for the background, while the integrals are evaluated in the range $0<t<t^{max}$ with $t^{max} \gg \tau_{eff}$. The τ_{eff} for the Mg_Eu_mix and Mg_Eu_span are 0.30±0.01 ms and 0.70±0.01 ms, respectively. This different behaviour can be explained by considering that for the Mg_Eu_mix sample the asymmetry ratio (4.36) is higher than for the Mg_Eu_span (3.84) and therefore the lower point symmetry of the Eu^{III} sites implies longer lifetimes of the $^5D_0$ level (if non-radiative relaxation processes as multiphonon relaxation processes are similar for the samples as in the present case). The emission decay behaviour for the Eu^{III} doped $Ca(OH)_2$ differs from that of $Mg(OH)_2$. In fact, in Eu^{III} doped $Ca(OH)_2$, the emission decay can be fit using two exponential curves, thus obtaining two different lifetimes: τ_1=0.035±0.001 ms and τ_2=0.277±0.001 ms. The τ_2 value is very similar to the one pertinent to europium hydroxide (0.22 ms),[68] thus confirming the presence of $Eu(OH)_3$ in Ca_Eu_mix NPs. As far as the τ_1 value is concerned, it is quite short and consistent with a slightly distorted site for Eu^{III} as well as a strong non-radiative relaxation due to the high energy phonons of the hydroxide ions surrounding the lanthanide ions. We tentatively assign this lifetime to Eu^{III} ions substituting the Ca^{II} ones in the $Ca(OH)_2$ lattice, substitution which is facilitated by the similarity of Ca^{II} (126 pm, in eight-fold coordination) and Eu^{III} (120.6 pm, in eight-fold coordination) ionic radii.[69, 70]

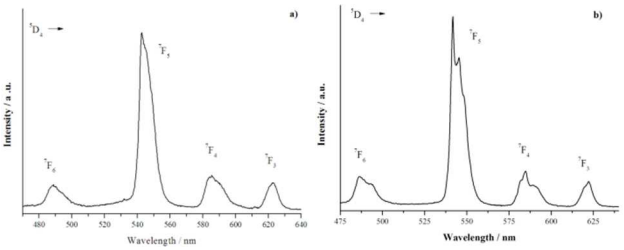

Fig. 10 Room temperature emission spectrum of Mg_Tb_span (a) and Mg_Tb_mix (b)

The same experiment was carried out on Tb-doped systems. RT emission spectra of Mg_Tb_span and Mg_Tb_mix samples upon laser excitation at 355 nm are shown in Figure 10 in the 470-640 nm wavelength range. The emission bands can be assigned to $^5D_4 \rightarrow {}^7F_J$ (J=6, 5, 4, 3, see also Figure E.S.I. 7b) transitions typical of the Tb^{III} ion. Both the spectra are dominated by the $^5D_4 \rightarrow {}^7F_5$ emission bands. Analogously to Eu^{III} doped samples bands are quite broad, suggesting even for Tb^{III} ions, a significant structural disorder around them. In Figure 11 Mg_Eu_mix and Mg_Tb_mix samples are shown, evidencing the bright Eu^{III} and Tb^{III} emission upon excitation with UV radiation. It is worth noting that the energy gap between the $^5D_0$ emitting level of the Eu^{III} ions and the next lower lying energy one is around 12000 cm^{-1} and therefore the non-radiative multiphonon relaxation processes are not extremely efficient for the present hydroxide hosts. The luminescence efficiency is most probably better for the Tb^{III} doped samples as the energy gap between the $^5D_4$ emitting level and the next lower lying energy one is around 15000 cm^{-1}.

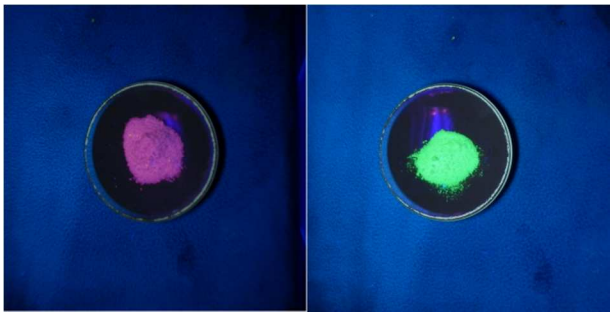

Fig. 11 Mg_Eu_mix (left) and Mg_Tb_mix (right) samples irradiated with UV radiation.

Conclusions

In this contribution an easy, reproducible, fast and effective method to prepare nanocrystalline pure and doped magnesium and calcium hydroxides NPs which crystallise already at room temperature, without any need of successive thermal treatment, was optimised and described. This approach affords a very precise control on the stoichiometry, structure and size of the obtained NPs. The MEs method allowed to achieve polycrystalline powder with an average crystallite size ~ 20 nm for $Mg(OH)_2$ systems and ~ 35 nm for $Ca(OH)_2$ systems, without particular difference between pure and doped NPs. The NPs characterisation was carried out by exploiting different and complementary techniques. The role of the used surfactant (or mixture thereof) on the stability of the achieved suspension and on the final features of the nanostructures was assessed. As far as the functionality of the addressed systems is concerned, no significant cytotoxicity or influence on the viability of ES2 cells was revealed after 48 hours of culture, regardless of NPs concentration and doping. The absence of cytotoxic effects and the good luminescence performances of Eu^{III} (in the red) and Tb^{III} (in the green) doped magnesium and calcium hydroxides candidates these materials for in-vitro and in-vivo fluorescence imaging. In particular, this kind of nanoparticles represents a promising tool for cell monitoring over prolonged experimental time thanks to the long-term stability of the nanoparticles in physiological conditions.

Acknowledgements

The University of Padua, Italy and the Italian National Research Council (CNR) are acknowledged for financial support. Prof. Fabrizio Mancin (Dipartimento di Scienze Chimiche, Università degli Studi di Padova) is gratefully acknowledged for DLS measurements. Dr. Roberta Saini (Dipartimento di Scienze Chimiche, Università degli Studi di Padova) is gratefully thanked for TGA-DSC measurements. Dr. Massimiliano Rocchia and Thermo Fischer are gratefully acknowledged for help in recording and processing Raman data. A.M and F.B. are grateful to Dr. Cristina Foss (University of Trento and BIOTech Lab) for performing LDH and Alamar Blue tests. A.S. and M.P. acknowledge Fondazione Cariverona (Verona, Italy), project Verona Nanomedicine Initiative, for financial support.

References

1. T. M. Fahmy, P. M. Fong, J. Park, T. Constable and W. M. Saltzman, *AAPS J.*, 2007, **9**, E171-E180.
2. V. J. Pansare, S. Hejazi, W. J. Faenza and R. K. Prud'homme, *Chem. Mater.*, 2012, **24**, 812-827.
3. J.-C. G. Bünzli, *Chem. Rev.*, 2010, **110**, 2729-2755.
4. P. Sharma, S. Brown, G. Walter, S. Santra and B. Moudgil, *Adv. Colloid Interface Sci.*, 2006, **123-126**, 471-485.
5. K. Landfester, A. Musyanovych and V. Mailaender, *J. Polym. Sci., Part A: Polym. Chem.*, 2010, **48**, 493-515.
6. V. Biju, T. Itoh, A. Anas, A. Sujith and M. Ishikawa, *Anal. Bioanal. Chem.*, 2008, **391**, 2469-2495.
7. Y. Su, F. Peng, Z. Jiang, Y. Zhong, Y. Lu, X. Jiang, Q. Huang, C. Fan, S.-T. Lee and Y. He, *Biomaterials*, 2011, **32**, 5855-5862.
8. A. Llevot and D. Astruc, *Chem. Soc. Rev.*, 2012, **41**, 242-257.
9. S. J. Soenen, P. Rivera-Gil, J.-M. Montenegro, W. J. Parak, S. S. C. De and K. Braeckmans, *Nano Today*, 2011, **6**, 446-465.
10. N. Khlebtsov and L. Dykman, *Chem. Soc. Rev.*, 2011, **40**, 1647-1671.
11. C. Martinez-Boubeta, L. Balcells, R. Cristofol, C. Sanfeliu, E. Rodriguez, R. Weissleder, S. Lope-Piedrafita, K. Simeonidis, M. Angelakeris, F. Sandiumenge, A. Calleja, L. Casas, C. Monty and B. Martinez, *Nanomedicine (Philadelphia, PA, U. S.)*, 2010, **6**, 362-370.
12. F. Tamimi, N. D. Le, D. C. Bassett, S. Ibasco, U. Gbureck, J. Knowles, A. Wright, A. Flynn, S. V. Komarova and J. E. Barralet, *Acta Biomater.*, 2011, **7**, 2678-2685.
13. Y. Yu, J. Wang, C. Liu, B. Zhang, H. Chen, H. Guo, G. Zhong, W. Qu, S. Jiang and H. Huang, *Colloids Surf., B*, 2010, **76**, 496-504.
14. A. Doat, F. Pelle, N. Gardant and A. Lebugle, *J. Solid State Chem.*, 2004, **177**, 1179-1187.
15. H.-C. Huang, S. Barua, G. Sharma, S. K. Dey and K. Rege, *J. Controlled Release*, 2011, **155**, 344-357.
16. F. Chen, Y.-J. Zhu, K.-H. Zhang, J. Wu, K.-W. Wang, Q.-L. Tang and X.-M. Mo, *Nanoscale Res. Lett.*, 2011, **6**, 67, 69 pp.
17. V. Sokolova and M. Epple, *Angew. Chem., Int. Ed.*, 2008, **47**, 1382-1395.
18. P. J. Neuvonen and K. T. Kivisto, *Eur. J. Clin. Pharmacol.*, 1988, **35**, 495-501.
19. T. Okiji and K. Yoshiba, *Int J Dent*, 2009, **2009**, 464280.
20. X. Gao, M. Hu, L. Lei, D. O'Hare, C. Markland, Y. Sun and S. Faulkner, *Chem. Commun. (Cambridge, U. K.)*, 2011, **47**, 2104-2106.
21. C. Bouzigues, T. Gacoin and A. Alexandrou, *ACS Nano*, 2011, **5**, 8488-8505.
22. K. Landfester, N. Bechthold, F. Tiarks and M. Antonietti, *Macromolecules*, 1999, **32**, 5222-5228.
23. F. J. Schork, Y. Luo, W. Smulders, J. P. Russum, A. Butte and K. Fontenot, *Adv. Polym. Sci.*, 2005, **175**, 129-255.
24. M. Antonietti and K. Landfester, *Prog. Polym. Sci.*, 2002, **27**, 689-757.
25. A. Ethirajan and K. Landfester, *Chem. - Eur. J.*, 2010, **16**, 9398-9412.
26. K. Landfester, *Angew. Chem., Int. Ed.*, 2009, **48**, 4488-4507.
27. R. Muñoz-Espì, C. K. Weiss and K. Landfester, *Curr. Opin. Colloid Interface Sci.*, 2012, **17**, 212-224.
28. R. Muñoz-Espì, Y. Mastai, S. Gross and K. Landfester, *CrystEngComm*, 2013, **15**, 2175-2191.
29. P. Dolcet, M. Casarin, C. Maccato, L. Bovo, G. Ischia, S. Gialanella, F. Mancin, E. Tondello and S. Gross, *J. Mater. Chem.*, 2012, **22**, 1620-1626.
30. P. Dolcet, F. Latini, M. Casarin, A. Speghini, E. Tondello, C. Foss, S. Diodati, L. Verin, A. Motta and S. Gross, *Eur. J. Inorg. Chem.*, 2013, **2013**, 2291-2300.
31. M. Willert, R. Rothe, K. Landfester and M. Antonietti, *Chem. Mater.*, 2001, **13**, 4681-4685.
32. A. Taden, M. Antonietti, A. Heilig and K. Landfester, *Chem. Mater.*, 2004, **16**, 5081-5087.
33. C. Saiwan, S. Krathong, T. Anukulprasert and E. A. O'Rear, III, *J. Chem. Eng. Jpn.*, 2004, **37**, 279-285.
34. M. Hajir, P. Dolcet, V. Fischer, J. Holzinger, K. Landfester and R. Munoz-Espi, *J. Mater. Chem.*, 2012, **22**, 5622-5628.
35. F. Caruso, *Colloids and Colloid Assemblies - Synthesis, Modification, Organization and Utilization of Colloid Particles, 1st Ed.*, Wiley-VCH, Weinheim, 2004.
36. B. S. Zolnik, A. Gonzalez-Fernandez, N. Sadrieh and M. A. Dobrovolskaia, *Endocrinology*, 2010, **151**, 458-465.
37. G. Baier, A. Cavallaro, K. Friedemann, B. Müller, G. Glasser, K. Vasilev and K. Landfester, *Nanomed. Nanotech. Biol. Med.*, 2014, **10**, 131-139.
38. M. Fichter, G. Baier, M. Dedters, L. Pretsch, A. Pietrzak-Nguyen, K. Landfester and S. Gehring, *Nanomed. Nanotech. Biol. Med.*, 2013, **9**, 1223-1234.
39. K. Landfester, M. Willert and M. Antonietti, *Macromolecules*, 2000, **33**, 2370-2376.
40. D. Briggs and M. P. Seah, *Practical Surface Analysis - Volume 1 - Auger and X-ray Photoelectron Spectroscopy, 2nd Ed.*, John Wiley & Sons, New York, 1990.
41. D. A. Shirley, *Phys. Rev. B*, 1972, **5**, 4709-4713.
42. J. F. Moulder, W. F. Stickle, P. E. Sobol and K. D. Bomben, *Handbook of X-Ray Photoelectron Spectroscopy - A Reference Book*

of Standard Spectra for Identification and Interpretation of XPS Data, Perkin-Elmer Corp., Eden Prarie, Minnesota, 1992.
43. H. P. Klug and L. E. Alexander, *X-Ray Diffraction Procedures for Polycrystalline and Amorphous Materials*, J. Wiley & Sons, New York, 1974.
44. T. L. Barr and S. Seal, *J. Vac. Sci. Technol., A*, 1995, **13**, 1239-1246.
45. M. R. Alexander, S. Payan and T. M. Duc, *Surf. Interface Anal.*, 1998, **26**, 961-973.
46. R. Xu and H. C. Zeng, *Langmuir*, 2004, **20**, 9780-9790.
47. M. J. Capitàn, M. A. Centeno, P. Malet, I. Carrizosa, J. A. Odriozola, A. Marquez and S. J. Fernandez, *J. Phys. Chem.*, 1995, **99**, 4655-4660.
48. P. Ghods, O. B. Isgor, J. R. Brown, F. Bensebaa and D. Kingston, *Appl. Surf. Sci.*, 2011, **257**, 4669-4677.
49. D. E. Haycock, C. J. Nicholls, D. S. Urch, M. J. Webber and G. Wiech, *J. Chem. Soc., Dalton Trans.*, 1978, 1791-1796.
50. S. Ardizzone, C. L. Bianchi, M. Fadoni and B. Vercelli, *Appl. Surf. Sci.*, 1997, **119**, 253-259.
51. T. Sugama, L. E. Kukacka, N. Carciello and N. J. Hocker, *Cem. Concr. Res.*, 1989, **19**, 857-867.
52. G. Socrates, *Infrared and Raman Characteristic Group Frequencies: Tables and Charts, 3rd Ed.*, John Wiley & Sons, Chichester, UK, 2004.
53. G. Gouadec and P. Colomban, *Prog. Cryst. Growth Charact. Mater.*, 2007, **53**, 1-56.
54. G. Gouadec and P. Colomban, *J. Raman Spectrosc.*, 2007, **38**, 598-603.
55. R. Frech, E. C. Wang and J. B. Bates, *Spectrochim. Acta, Part A*, 1980, **36A**, 915-919.
56. K. Suito, J. Namba, T. Horikawa, Y. Taniguchi, N. Sakurai, M. Kobayashi, A. Onodera, O. Shimomura and T. Kikegawa, *Am. Mineral.*, 2001, **86**, 997-1002.
57. D. Nave, S. Rosenwaks, R. Vago and I. Bar, *J. Appl. Phys.*, 2004, **95**, 8309-8313.
58. A. Aminzadeh, *Spectrochim. Acta, Part A*, 1997, **53A**, 693-697.
59. S. Martinez-Ramìrez and M. Frias, *Appl. Clay Sci.*, 2011, **51**, 283-286.
60. P. S. Braterman and R. T. Cygan, *Am. Mineral.*, 2006, **91**, 1188-1196.
61. V. Drozd, S. Saxena, S. V. Garimella and A. Durygin, *Int. J. Hydrogen Energy*, 2007, **32**, 3370-3375.
62. E. Riedel, *Anorganische Chemie*, Walter de Gruyter, Berlin, 1994.
63. R. Reisfeld, E. Zigansky and M. Gaft, *Mol. Phys.*, 2004, **102**, 1319-1330.
64. Q. G. Zeng, Z. J. Ding, Z. M. Zhang and Y. Q. Sheng, *J. Phys. Chem. C*, 2010, **114**, 4895-4900.
65. R. L. Cone and R. Faulhaber, *J. Chem. Phys.*, 1971, **55**, 5198-5206.
66. R. D. Peacock, *Struct. Bonding*, 1975, **22**, 83-122.
67. S. Shionoya and W. M. Yen, *Phosphor Handbook, 1st Ed.*, CRC Press, Boca Raton, FL, 1999.
68. I. Pointeau, B. Piriou, M. Fedoroff, M.-G. Barthes, N. Marmier and F. Fromage, *J. Colloid Interf. Sci.*, 2001, **236**, 252-259.
69. *WebElements: the periodic table on the web,* http://www.webelements.com/.
70. *Shannon Radii - Atomistic Simulation Group,* http://abulafia.mt.ic.ac.uk/shannon/ptable.php.

